


# MISSION-PROFILE-BASED HYBRID POWER SYSTEM DESIGN AND OPTIMIZATION FOR VTOL AIRCRAFT IN REGIONAL AIR MOBILITY

Guangjun Shen[1], Xiaobo Zhang[1], Wang Hao[1], Zhanxue Wang[1]

[1]School of Power and Energy, Northwestern Polytechnical University, Xi'an 710072, China

## Abstract

Vertical take-off and landing aircraft are a key enabler for regional air mobility. However, the combination of high-power demands during vertical take-off and high-energy requirements during cruise poses a significant challenge to propulsion system design. This paper proposes a mission-based sizing optimization framework for a turboshaft-based series hybrid electric propulsion system. Based on a turboshaft thermodynamic model, it integrates fuel-burn-induced aircraft mass variation and turboshaft-generator operation strategy optimization within a unified time-stepping simulation. The framework is then applied to the propulsion system design of a RAM-oriented tiltrotor aircraft with a take-off gross weight of 1900 kg and a range of 500 km. The results show that compared with a conventional fixed-mass sizing method with simplified engine modeling, the framework effectively mitigates component oversizing, yielding a 12.7 kg reduction in system mass. This improvement is primarily attributed to improved power demand prediction enabled by mission-driven mass evolution and optimized turboshaft–generator operating strategies that reduce peak battery power demand. Further analysis reveals that battery sizing is governed by peak discharge C-rate, while generator sizing exhibits a trade-off between system mass and efficiency. Overall, the proposed framework enhances sizing accuracy by capturing the coupled effects of mass variation and operational strategy optimization.

**Keywords:** vertical take-off and landing aircraft; hybrid-electric propulsion; sizing; powertrain optimization

## 1. Introduction

### 1.1 Context

Vertical Take-Off and Landing (VTOL) aircraft, as a core platform within the advanced air mobility ecosystem, exhibit significant application potential in Regional Air Mobility (RAM) missions [1,2]. The typical mission profiles, comprising take-off, transition, and cruise phases, exhibit strongly phase-dependent power and energy requirements: the vertical take-off and transition phases are dominated by peak power demand, whereas the cruise phase is characterized by dominant energy demand. This coupled requirement for both high power density and high energy density imposes stringent challenges on the conceptual design of propulsion systems [3]. Although all-electric propulsion architectures offer advantages such as high efficiency and zero emissions, they are fundamentally constrained by the relatively low specific energy of current lithium-ion battery technologies (200–300 Wh/kg) [4–6]. As a result, they face inherent limitations in range capability and payload capacity when applied to long-endurance RAM missions. Conventional fuel-based propulsion systems, while possessing superior energy density, exhibit inherent drawbacks in direct-drive configurations, particularly the severe engine oversizing required for vertical take-off and the consequent degradation in part-load efficiency during cruise. To reconcile the complementary advantages of these two energy paradigms, the turboshaft-based series hybrid electric propulsion system (TS-SHEPS) has emerged as a key development direction [7]. Owing to the mechanical decoupling between the propulsion system and the thermal engine, the architecture relaxes the coupling between engine operating conditions and load demands, thereby enabling increased flexibility in mission-driven system-level optimization.

In the field of conceptual design for hybrid electric propulsion systems (HEPS), system sizing and

parameter matching have attracted considerable attention in recent years. Friedrich et al. [8] conducted component-level sizing for light fixed-wing aircraft by integrating aerodynamic characteristics of the vehicle with propulsion system mass estimation. Li et al. [9] developed a coordinated design framework applicable to VTOL propulsion systems by introducing multi- domain parameters, enabling mission-driven configuration selection and parameter matching. Dehghani et al. [10] further proposed a hybrid energy storage series propulsion system sizing and matching methodology composed of batteries, supercapacitors, and an engine–generator set, effectively mitigating the issue of excessive battery discharge rates induced by pulsed high peak power demand. To capture the effects of fuel consumption–induced mass variation and energy management strategies on system sizing, time-stepping simulation and energy management strategy optimization have been introduced into the design process. Zong et al. [11] incorporated a fuel correction factor into power estimation to dynamically account for aircraft mass variation due to fuel burn. Meng et al. [12] integrated propulsion system sizing with energy management strategies and proposed a dual-loop sizing methodology based on optimal power allocation, achieving coupled optimization of component sizing and energy management strategy. To improve the fidelity of component-level modeling, Jiang et al. [13] investigated the modeling and control of a turboelectric propulsion system. A high-fidelity thermodynamic model was developed using a component-based, object-oriented approach, achieving a deviation of only 0.22% compared with commercial software. Yi et al. [14] adopted the component method to establish thermodynamic models for rotors and variable-speed power turbines, and verified that combined speed regulation reduces fuel consumption by approximately 5%.

However, several key limitations remain. Most existing sizing approaches neglect the dynamic variation of aircraft gross weight caused by continuous fuel consumption, which may introduce cumulative errors in power demand estimation and component sizing, particularly for long-endurance missions. Simplified engine performance maps and fixed-efficiency generator models are still widely adopted, limiting the fidelity of system-level performance representation. In addition, engine performance modeling has not yet been integrated into mission-based sizing and optimization frameworks for hybrid-electric propulsion systems.

To address the aforementioned issues, a Fuel-Burn-Aware Mission-Based Sizing Optimization (FMOSO) framework for TS-SHEPS is developed. The proposed framework integrates flight mission profile, fuel-burn-induced aircraft mass variation, turboshaft-generator operation strategy optimization within a unified time-stepping iterative process. During the mission simulation, aircraft mass is continuously updated according to fuel consumption, and the corresponding power demand is simultaneously corrected, thereby establishing a closed-loop coupling among fuel consumption, aircraft mass evolution, power requirement, and propulsion system operating states. The proposed framework is subsequently applied to a RAM-oriented tiltrotor aircraft under a representative mission profile. An adaptive multi-strategy differential evolution algorithm is introduced to perform the system sizing optimization.

The paper is organized as follows: Section 2 develops the performance and mass estimation models of TS-SHEPS components. Section 3 focuses on the turboshaft–generator subsystem, establishing a flight-phase-based adaptive operating mode matching mechanism and developing operational strategy optimization methods for two operating modes. Section 4 presents the fuel-burn-aware mission-based sizing optimization framework. Section 5 formulates the system-level component sizing optimization problem and evaluates the performance of the proposed FMOSO framework against the conventional design method. Section 6 concludes the paper by summarizing the main findings and their implications.

## 2. Component Performance Modeling and Mass Evaluation

### 2.1 TS-SHEPS Architecture

The overall system architecture of the TS-SHEPS is illustrated in Figure 1. The propulsion system adopts a fully electric power transmission architecture, thereby achieving mechanical decoupling between the prime mover and the propulsive system. Functionally, the system can be divided into three subsystems: the turboshaft–generator subsystem (TGS), the battery energy storage subsystem (BESS), and the electric propulsion subsystem (EPS). These subsystems are connected

via a common DC bus, which supports power exchange, coordinated energy management, and system-level power distribution among multiple energy sources and loads. [15].

The TGS consists of a fuel tank, a turboshaft engine, a generator, and a rectifier. Fuel chemical energy is converted into mechanical power by the turboshaft engine and subsequently into electrical power by the generator. After rectification, the generated power is supplied to the DC bus. The BESS comprises a battery pack and a bidirectional DC/DC converter, enabling bidirectional energy exchange between the battery and the DC bus. The EPS consists of DC/AC inverters, electric motors, and propellers. Electrical power from the DC bus is converted and delivered to the motors, which drive the propellers to generate thrust.

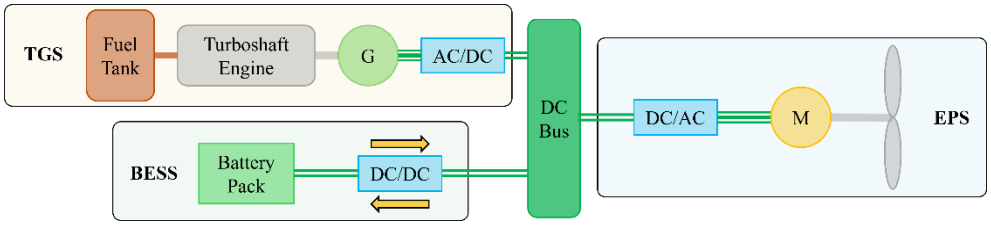



Figure 1 – TS-SHEPS architecture.

## 2.2 Component Performance Modeling

### *2.2.1 Component-Level Thermodynamic Model of the Turboshaft Engine*

The turboshaft engine considered in this study has a rated power range of 150–250 kW. Based on its power class and established statistical design trends reported in Ref. [16], a single-spool gas generator combined with a free power turbine configuration is adopted. A single-stage centrifugal compressor is selected to achieve a higher stage pressure ratio and improved aerodynamic efficiency under low mass flow conditions. Due to the manufacturing limitations associated with internal cooling passages in small-scale turbine blades, no internal cooling structures are considered. Under this assumption, the turbine inlet total temperature (i.e., combustor exit total temperature) can be maintained at approximately 1300 K [16].

To enable performance evaluation and component-level matching analysis of the turboshaft engine, a thermodynamics-based steady-state component-level simulation model is developed. The Tool for the Modeling and Analysis of Turbine Engine Systems (TMATS) [17] is used to develop the turboshaft engine model. The original computational workflow of TMATS is modified to accommodate the specific characteristics of the turboshaft engine. The design point computation workflow is illustrated in Figure 2. In this procedure, the exhaust duct pressure ratio is typically prescribed first, and the power turbine output is then determined based on the gas generator turbine exit conditions.

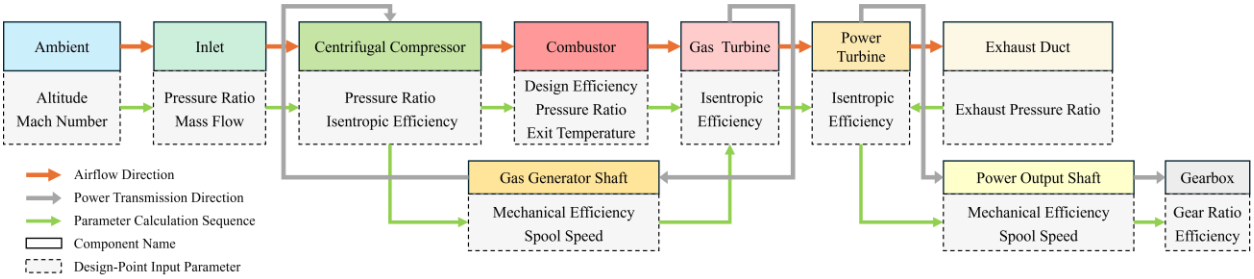



Figure 2 – Design point computation workflow for the turboshaft engine.

### *2.2.2 Efficiency Map-Based Model of the Generator*

The generator model is developed based on a speed–torque–efficiency characteristic map to capture its performance under varying operating conditions. To enhance model generality, a two-dimensional efficiency map is constructed using normalized rotational speed and torque. For any given operating point, the generator efficiency is obtained via two-dimensional interpolation of the characteristic map. The normalized efficiency map adopted from Ref. [18] is illustrated in Figure 3. Based on the relationship between the design-point parameters of the target generator and those of the reference

efficiency map, scaling factors for rotational speed and torque can be derived. These scaling factors are then used to rescale the map, enabling the transfer of performance characteristics across generators of different power ratings.

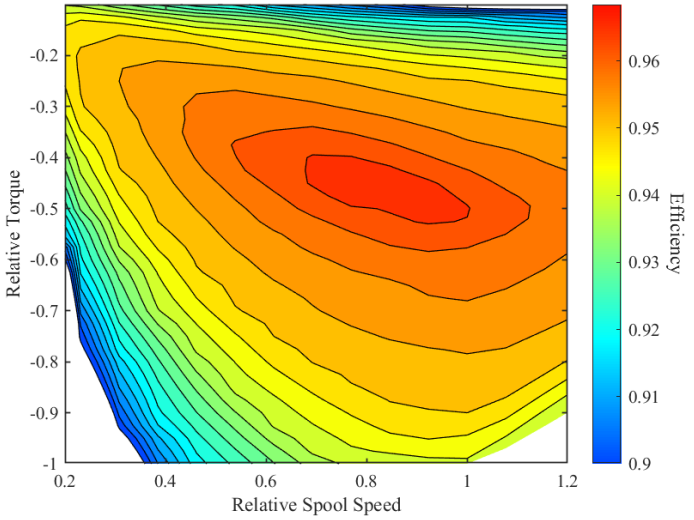



Figure 3 – Generator speed–torque–efficiency map.

The scaling factors are calculated as follows:

$$\begin{cases} S_n = \dfrac{n_{\text{des}}}{n_{\text{ref}}} \\ S_T = \dfrac{T_{\text{des}}}{T_{\text{ref}}} \end{cases} \tag{1}$$

where $S_n$ and $S_T$ are the rotational speed and torque scaling factors, respectively; $n_{\text{des}}$ and $T_{\text{des}}$ are the design-point rotational speed and torque of the target generator, respectively; and $n_{\text{ref}}$ and $T_{\text{ref}}$ are the corresponding design-point rotational speed and torque associated with the baseline efficiency characteristic map.

### 2.2.3 Second-Order RC Equivalent Circuit Model of the Battery

Common battery modeling approaches include electrochemical models, equivalent circuit models, and data-driven models [19–21]. Considering the trade-off among model fidelity, computational complexity, and engineering applicability, a second-order RC equivalent circuit model is adopted in this study for battery representation.

The battery terminal voltage can be expressed as:

$$V_{\text{bat}} = OCV(\text{SOC}) - IR_0 - V_1 - V_2 \tag{2}$$

The dynamics of the polarization branches can be described as:

$$\begin{cases} \dot{V}_1 = -\dfrac{1}{R_1 C_1} V_1 + \dfrac{I}{C_1} \\ \dot{V}_2 = -\dfrac{1}{R_2 C_2} V_2 + \dfrac{I}{C_2} \end{cases} \tag{3}$$

The SOC is calculated using the ampere-hour counting method:

$$\text{SOC}_{(t)} = \text{SOC}_{(0)} - \frac{\int I\,dt}{Q_{\text{bat}}} \tag{4}$$

where $R_0$ is the ohmic resistance; $R_1$, $R_2$ are the polarization resistances; $C_1$, $C_2$ are the polarization capacitance; and $Q_{\text{bat}}$ is the nominal capacity of the battery.

To satisfy practical engineering requirements, battery systems are typically constructed by configuring multiple cells in series–parallel arrangements to form packs.

### 2.2.4 Piecewise Efficiency Model of the EPS

In this study, high-fidelity electromagnetic models of the electric motor and aerodynamic models of the rotor are not considered. Instead, component performance is represented using phase-dependent efficiency parameters derived from Ref. [22] and adjusted to the target propulsion system. The corresponding efficiency assumptions are listed in Table 1.

Table 1 – Efficiency parameters of EPS components under different flight phases.

| Parameter | Definition | hover | Climb/Descent | Cruise |
|---|---|---|---|---|
| $PL_{\text{hover}}$ | Hover power loading | 5 kg/kW | — | — |
| $\eta_{\text{cab}}$ | Cable efficiency | 0.99 | 0.99 | 0.99 |
| $\eta_{\text{inv}}$ | Inverter efficiency | 0.97 | 0.97 | 0.97 |
| $\eta_{\text{motor}}$ | Motor efficiency | 0.94 | 0.95 | 0.96 |
| $\eta_{\text{rotor}}$ | Rotor propulsive efficiency | — | 0.85 | 0.85 |

## 2.3 Component Mass Estimation

Mass estimation is limited to the TGS and the BESS. Specifically, the mass of the turboshaft engine and electric generator is determined on the basis of existing literature, with the turboshaft engine mass estimated via Ref. [23] and the electric generator mass extracted from Ref. [24]. Other components are evaluated comprehensively based on the state-of-the-art component technical level and industry lightweight development tendency. Detailed mass estimation parameters of all components are summarized in Table 2.

Table 2 – Parameters for component mass estimation.

| Component | Method | Formulation | Key Parameter |
|---|---|---|---|
| Turboshaft engine | Empirical scaling law | $0.625(P+200)^{0.8}$ | — |
| Generator | Power density | $P_{\text{peak}} / \alpha_{\text{P,peak}}$ | $\alpha_{\text{P,peak}}$=10kW/kg |
| AC/DC | Power density | $P / \alpha_P$ | $\alpha_P$=12kW/kg |
| Fuel | Integration | $\gamma_{\text{fuel}} \int_0^{t_{\text{mission}}} W_f(t)dt$ | $\gamma_{\text{fuel}}$=1.25 (reserve margin factor) |
| Battery pack | Power density | $E_{\text{pack}} / \alpha_E \cdot \gamma$ | $\alpha_E$=300Wh/kg<br>$\gamma$=1.1 (packaging factor from cell to pack) |
| DC/DC | Energy density | $P / \alpha_P$ | $\alpha_P$=12kW/kg |

# 3. Mission-Driven Energy Management and TGS Operating Strategy Optimization

## 3.1 Mission-Based Operating Modes and Energy Management Strategy

To enable tractable system-level analysis, the operating behavior of the TS-SHEPS over the mission profile is discretized in time and represented using a finite set of representative operating modes. Based on this abstraction, an FSM-based energy management strategy is established. The resulting discrete operating mode set consists of five characteristic modes:

S1: Ground Idle Mode. The TS-SHEPS operates in a pre-takeoff ground idle condition. The TGS maintains a safe idle point, while the BESS remains inactive, not participating in power regulation.

S2: Maximum Continuous Power (MCP) Mode. During high-power mission segments, the TS-SHEPS operates near the maximum continuous power limit. The TGS delivers MCP, and the BESS discharges concurrently to supply additional electrical power.

S3: Cruise Power-Following Mode. In cruise operation without battery charging, the TGS is regulated within a high-efficiency region to meet the propulsion power demand. The BESS remains inactive to minimize cycling losses, maintaining SOC at a level.

S4: Cruise Charging Mode. During the cruise phase, the TGS is scheduled to operate at its design

point, supplying the required propulsion power and simultaneously providing excess electrical power to charge the BESS.

S5: Descent Idle Mode. The TGS is reduced to a low-load operating mode, providing only the minimum power. The BESS enters a thermal management protection state and does not participate in power exchange.

To achieve adaptive mode transitions, an FSM-based energy management strategy is developed to coordinate the operation of the TGS and BESS. Mode transitions are governed by SOC thresholds and power demand derived from mission phase segmentation, enabling structured power allocation and operating mode scheduling under different flight conditions.

Based on the FSM mode-space, transitions between operating modes are determined by rule-based deterministic functions. The system input vector is defined as

$$U(t)=\left[Phase(t),\ \mathrm{SOC}(t)\right]^{T} \tag{5}$$

where *Phase* denotes the current flight mission phase identifier. The corresponding mode transition logic is illustrated in Figure 4.

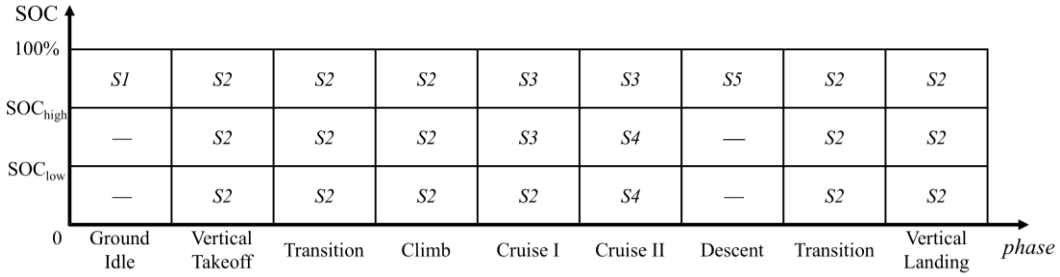



Figure 4 – Energy management strategy based on FSM

## 3.2 TGS Maximum Continuous Power Operation Strategy Optimization

When the system operates in mode S2, the TGS is required to deliver maximum electrical power output. However, as discussed previously, the MCP operating mode of the turboshaft engine does not necessarily correspond to the maximum continuous operating mode of the overall TGS. This discrepancy arises because generator efficiency exhibits nonlinear dependence on rotational speed and torque, causing the overall power-generation efficiency to vary across feasible operating conditions. Consequently, the TGS operating point should be determined through a system-level matching process that simultaneously accounts for engine performance characteristics, generator efficiency variations, and component operating constraints.

The optimization problem of the MCP operating strategy for the TGS can be formulated as follows:

$$\begin{aligned} &\max_{N_{\mathrm{gen}},T_{\mathrm{gen}}} P_{\mathrm{elec}}(N_{\mathrm{gen}},T_{\mathrm{gen}}) \\ &\text{s.t.}\quad \begin{cases} R(s)\le R_{\mathrm{set}} \\ s\in\Omega_{\mathrm{eng}},\quad (N_{\mathrm{gen}},T_{\mathrm{gen}})\in\Omega_{\mathrm{gen}} \end{cases} \end{aligned} \tag{6}$$

In the above optimization problem, $x=[N_{\mathrm{gen}},T_{\mathrm{gen}}]$ denotes the optimization variables, where $N_{\mathrm{gen}}$ and $T_{\mathrm{gen}}$ are the rotational speed and torque of the generator, respectively. $P_{\mathrm{elec}}$ is electrical output power of TGS. The state vector $s$ is state parameters, used to characterize the coupled operating point of the engine. $R$ represents the residual vector of the engine thermodynamic balance equations and is constrained to satisfy a prescribed convergence tolerance. $\Omega_{\mathrm{eng}}$ denotes parameter constraints of the engine while $\Omega_{\mathrm{gen}}$ represents feasible operating region of the generator.

The differential evolution (DE) algorithm [25] is applied to optimize, as illustrated in Figure 5. The optimization is conducted under the parameter constraints of the engine as well as the operational constraints of the generator, thereby yielding the maximum continuous electrical power output of the TGS and its corresponding optimal operating point.

## 3.3 TGS Minimum Fuel Consumption Rate Operation Strategy Optimization

Similarly, the engine optimum-efficiency operating point does not necessarily coincide with the

system-level optimum operating point of the TGS. When the engine operates at its own optimum point, the generator may be forced to operate away from its high-efficiency region, leading to a reduction in electrical conversion efficiency and, consequently, an increase in system-level specific fuel consumption per unit electrical power output, highlighting the need for engine–generator matching optimization.

Under the S3 operating mode, minimum fuel consumption rate operation strategy optimization problem can be formulated as:

$$\min_{N_{\text{gen}},T_{\text{gen}}} \dot{m}_f(N_{\text{gen}},T_{\text{gen}}) \quad \text{s.t.} \begin{cases} P_{\text{elec}} = P_{\text{elec,set}} \\ R(s) \le R_{\text{set}} \\ s \in \Omega_{\text{eng}}, \quad (N_{\text{gen}},T_{\text{gen}}) \in \Omega_{\text{gen}} \end{cases} \tag{7}$$

Since the electrical power output in this operating mode is pre-defined, the optimization problem is essentially a coupled engine–generator matching problem under a fixed electrical power constraint. A state-space search method based on iso-power trajectories of the generator is proposed, as illustrated in Figure 5. First, the iso-power operating trajectory corresponding to the specified electrical power output is obtained from the generator performance model, from which candidate speed–torque pairs are derived. Subsequently, each candidate pair is used as an input to turboshaft engine off-design ponit calculation model, and the engine operating point is obtained through iterative convergence of the engine balance equations. For each candidate operating point, feasibility is evaluated against the engine constraints. Finally, among all feasible solutions, the optimal coupled operating point is determined by minimizing fuel consumption rate.

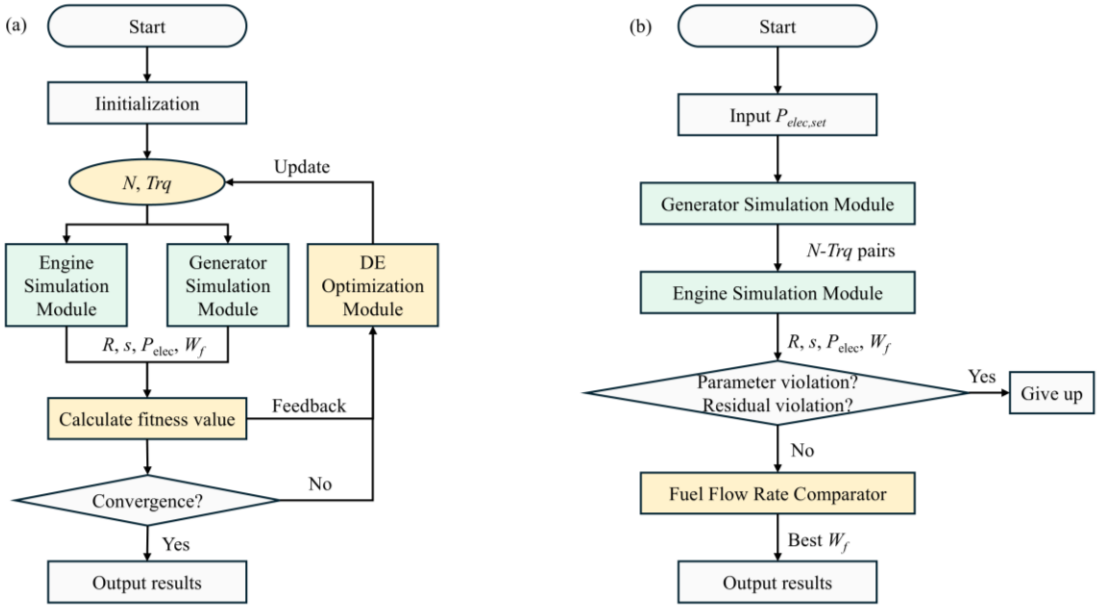



Figure 5 – TGS operating strategy optimization workflow: (a) maximum continuous power mode; (b) minimum fuel consumption rate mode

## 4. Fuel-Burn-Aware Mission-Based Sizing Optimization Framework

### 4.1 Time-Stepping Method under Mass Variation

During the execution of a prescribed mission profile, the operating mode of the TGS is jointly governed by the instantaneous aircraft mass, the power demand, and the energy management strategy. As fuel is consumed, the aircraft mass decreases continuously, which leads to a time-varying evolution of the required power demand. This variation in power demand further reshapes the operating mode of the TGS and BESS, thereby affecting the fuel consumption rate. As a result, a time-evolving coupled relationship is established throughout the mission execution process. The propagation mechanism can be summarized in Eq. (8).

$$m(t_k) \rightarrow P_{req}(t_k) \rightarrow S(t_k) \rightarrow W_f(t_k) \rightarrow m(t_{k+1}) \tag{8}$$

Within each time step, the aircraft state is assumed to be quasi-steady. Accordingly, the power demand is determined from the current aircraft mass and flight phase. The energy management strategy is then applied to determine the operating mode of the TGS and BESS. Based on engine performance calculations, the corresponding electrical power output and fuel consumption rate are obtained, while the BESS determines its output current. Finally, the aircraft mass and battery SOC are updated, and the system proceeds to the next time step.

$$\begin{cases} P_{\text{req}}(t_k) = f_{\text{Aero}}\left(m(t_k), Phase(t_k)\right) \\ [S_{\text{TGS}}(t_k), S_{\text{BESS}}(t_k)] = f_{\text{EMS}}(\text{SOC}(t_k), P_{\text{req}}(t_k)) \\ [P_{\text{TGS}}(t_k), W_f(t_k)] = f_{\text{TGS}}\left(C_{\text{TGS}}(S_{\text{TGS}}(t_k)), H(t_k), V(t_k)\right) \\ [P_{\text{BESS}}(t_k), I_{\text{BESS}}(t_k)] = f_{\text{BESS}}(S_{\text{BESS}}(t_k), P_{\text{TGS}}(t_k)) \\ m(t_{k+1}) = m(t_k) - W_f(t_k)\Delta t \\ \text{SOC}(t_{k+1}) = \text{SOC}(t_k) - I_{\text{BESS}}(t_k)\Delta t \end{cases} \tag{9}$$

where $P_{\text{req}}$ denotes aircraft power demand; $f_{\text{Aero}}$ is the power demand calculation function; $S_{\text{TGS}}$ represents operating mode of the TGS; $f_{\text{EMS}}$ denotes energy management strategy; $W_f$ is engine fuel mass flow rate; $C_{\text{TGS}}$ represents the state of the TGS; $H$ and $V$ denote altitude and velocity, respectively; $S_{\text{BESS}}$ represents operating mode of the BESS; and $I_{\text{BESS}}$ denotes the BESS current.

## 4.2 Optimization Framework

The fuel-burn-aware mission-based sizing optimization framework is illustrated in Figure 6. The overall sizing optimization framework consists of an outer-loop optimization process coupled with an inner-loop full mission profile simulation. Initially, the TS-SHPS sizing parameters and flight mission profile are specified, from which the initial aircraft mass is calculated. These parameters are then passed to the full mission profile simulation module for mission-level performance evaluation. Within the simulation module, a time-stepping approach is adopted throughout the entire mission profile. At each time step, the required electrical power is first determined according to the current flight phase and aircraft mass. The resulting power demand is subsequently delivered to the energy management system (EMS), which determines the operating modes of the TGS and BESS based on the current power requirement and battery pack SOC. According to the operating commands issued by the EMS, the TGS operating strategy optimization module determines the optimal operating point of the TGS and calculates the corresponding fuel flow rate and electrical power output. The fuel consumption is integrated over the current time step to update the aircraft mass. Simultaneously, the BESS simulation module receives both the TGS electrical power output and the assigned operating mode command, calculates the current, and updates the SOC through time integration. The updated aircraft mass and SOC are then fed back to the next time step, forming a closed-loop time-stepping simulation process over the entire mission profile. Upon completion of the mission simulation, the total fuel consumption and time-history state parameters are obtained. These results are subsequently passed to the fitness evaluation module, where system feasibility is assessed by examining constraint violations, sizing rationality, and fuel sufficiency throughout the mission. Penalty terms are imposed when infeasible operating conditions or constraint violations occur. The resulting fitness value is then returned to the optimization module to update the sizing parameters. To improve global search efficiency and convergence performance, an adaptive multi-strategy differential evolution algorithm proposed in Ref. [26] is employed as the system-level optimization tool. In this method, multiple mutation strategies are incorporated into a candidate pool, with selection probabilities adaptively updated based on historical performance, allowing the algorithm to adaptively select strategies during evolution. This optimization-simulation cycle is repeated until the convergence criterion is satisfied, after which the optimal sizing results are obtained.

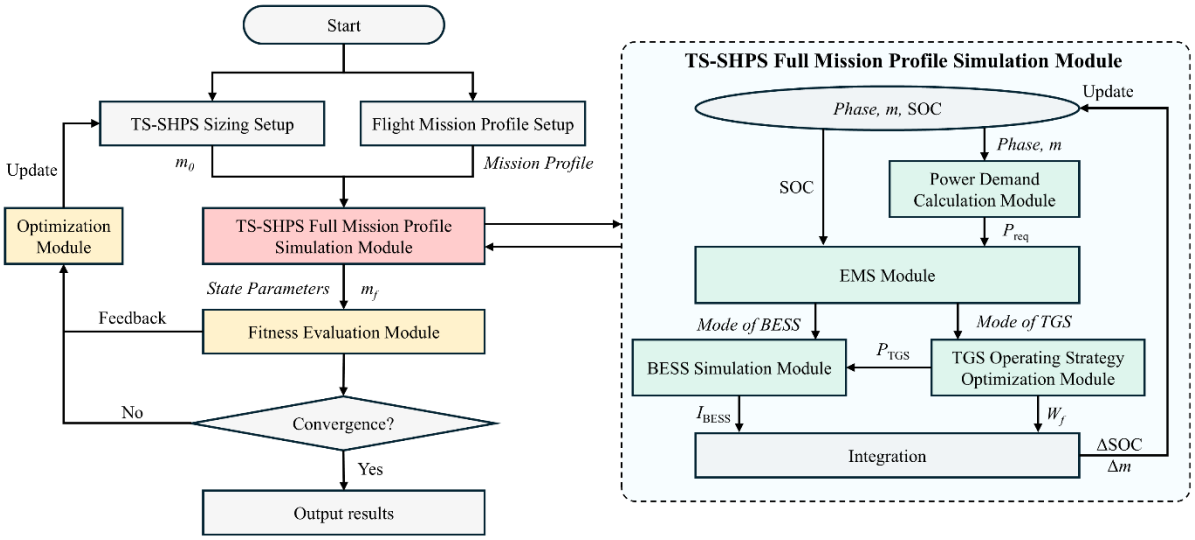



Figure 6 – Fuel-burn-aware mission-based sizing optimization framework.

## 5. TS-SHEPS Sizing Optimization and Result Analysis

### 5.1 Mission Profile Definition and Aircraft Parameter Setup

A representative VTOL mission profile reported in Ref. [22] is adopted as the baseline mission for the present study. The original mission was developed for a 800 km-class transport scenario. To align with the operational requirements of regional air mobility (RAM) applications [27], the mission range is adjusted to 500 km while maintaining the original mission structure. The resulting mission profile used for sizing is illustrated in Figure 7.

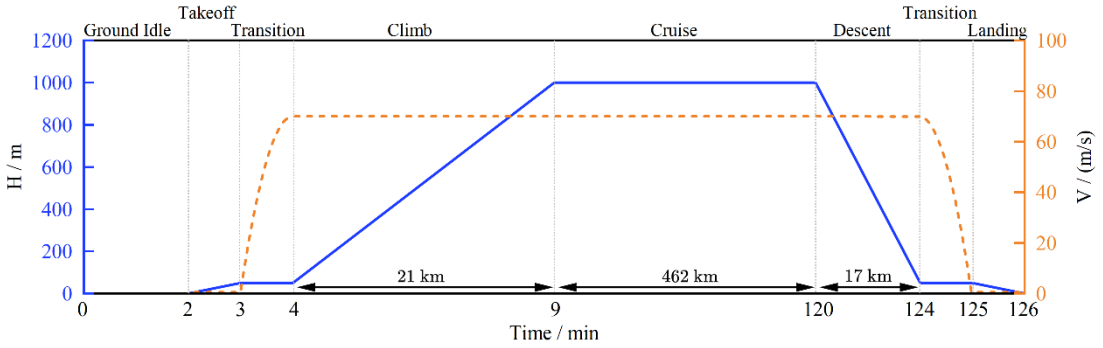



Figure 7 – Mission profile for 500 km RAM scenario.

To ensure consistency and comparability in the system-level sizing and optimization of the proposed SHPS, the Joby SHy4 hybrid-electric aircraft [28] is selected as the reference platform, as illustrated in Figure 8. The aircraft adopts a representative tiltrotor configuration with distributed electric propulsion, making it well suited for RAM applications. In the present study, the original propulsion architecture is replaced by the proposed TS-SHEPS, while the aerodynamic characteristics and airframe-related parameters of the reference aircraft are retained. The power demand is subsequently calculated using the methodology proposed in Ref. [22,29].

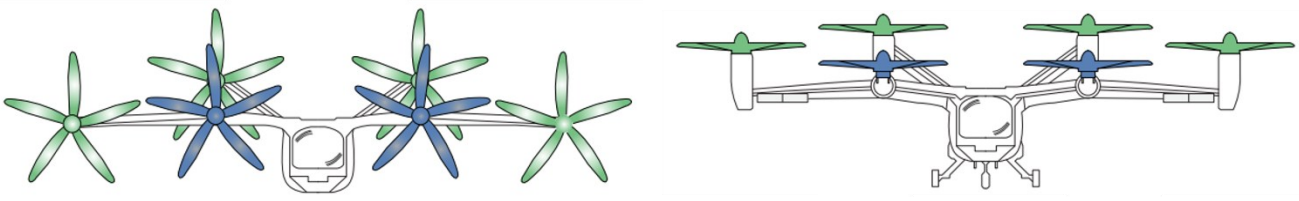


Figure 8 – Reference aircraft.

## 5.2 Optimization Problem Formulation

This study aims to identify the optimal sizing parameters of the TS-SHEPS through a system-level optimization framework. The objective is to minimize the total energy-system mass, defined as the sum of the TGS mass, BESS mass, and fuel onboard mass, while ensuring compliance with mission requirements and component operating constraints. A fixed takeoff mass strategy is adopted throughout the optimization process. Accordingly, reductions in energy-system mass are directly reflected as increases in available payload capacity, allowing payload performance to be evaluated implicitly rather than treated as an independent design variable. This assumption significantly simplifies the optimization procedure by eliminating the additional iterative loop typically required to resolve takeoff-mass consistency. Since the EPS is retained from the reference aircraft configuration, its mass has already been incorporated into the baseline structural mass and is therefore not included among the optimization variables.

The system-level sizing optimization problem can be formulated as follows:

$$
\begin{aligned}
&\min_{\mathbf{x}} J(\mathbf{x}) = m_{\mathrm{TGS}}(\mathbf{x}) + m_{\mathrm{BESS}}(\mathbf{x}) + m_{\mathrm{fuel}}(\mathbf{x}) \\
&\mathbf{x} = \left[ \pi_c, T_{t4}, P_{\mathrm{TGS,DP}}, n^*_{\mathrm{gen}}, \tau^*_{\mathrm{gen}}, N_s, N_p \right] \\
&\text{s.t.} \begin{cases}
\mathrm{TGS}: \begin{cases}
T_{t4} \le T_{t4,\max}, \quad SM_{\mathrm{comp}} \ge SM_{\min} \\
N_{\mathrm{HPS}} \le N_{r,\mathrm{HPS},\max}, N_{\mathrm{LPS}} \le N_{\mathrm{LPS},\max} \\
N_{c,\mathrm{comp}} \le N_{c,\mathrm{comp},\max}, N_{c,\mathrm{GT}} \le N_{c,\mathrm{GT},\max}, N_{c,\mathrm{PT}} \le N_{c,\mathrm{PT},\max} \\
T_{\mathrm{gen}} \le T_{\mathrm{gen},\max}, N_{\mathrm{gen}} \le N_{\mathrm{gen},\max}, \quad P_{\mathrm{gen,DP}} \le 0.85 P_{\mathrm{gen,peak}}
\end{cases} \\
\mathrm{BESS}: \begin{cases}
I_{\mathrm{cell,discharge}} \le I_{\mathrm{cell,discharge,max}}, I_{\mathrm{cell,charge}} \le I_{\mathrm{cell,charge,max}} \\
U_{\mathrm{cell,min}} \le U_{\mathrm{cell}} \le U_{\mathrm{cell,max}}
\end{cases}
\end{cases}
\end{aligned}
\tag{10}
$$

The definitions and bounds of the optimization variables are summarized in Table 3.

Table 3 – The definitions and bounds of the optimization variables.

| Variable | Variable Description | Lower Bound | Upper Bound |
|---|---|---|---|
| $\pi_c$ | compressor pressure ratio at design point (DP) | 6.0 | 9.5 |
| $T_{t4}$ | combustor exit temperature at DP | 1100K | 1300K |
| $P_{\mathrm{TGS},DP}$ | TGS output electric power at DP | 130kW | 180kW |
| $n^*_{\mathrm{gen}}$ | Relative rotational speed of generator at DP | 0.7 | 1 |
| $\tau^*_{\mathrm{gen}}$ | Relative torque of generator at DP | -0.9 | -0.4 |
| $N_s$ | series number of battery pack | 120 | 160 |
| $N_p$ | parallel number of battery pack | 10 | 40 |

The technological levels of the turboshaft engine components are adopted from Ref. [16]. The battery cell parameters are taken from Ref. [30]. The generator technology assumptions are based on Ref. [18]. The corresponding parameter settings are summarized inTable 4.

Table 4 – Parameter settings for TGS and BESS

| Parameter Description | Value | Parameter Description | Value |
|---|---|---|---|
| Inlet pressure ratio | 0.98 | AC/DC efficiency | 0.97 |
| Compressor isentropic efficiency (DP) | 0.8 | DC/DC efficiency | 0.98 |
| Combustor efficiency (DP) | 0.98 | Cell rated capacity | 3000mAh |
| Combustor pressure ratio | 0.95 | Cell rated voltage | 3.6V |
| Gas turbine isentropic efficiency (DP) | 0.84 | Cell operating voltage range | 2.5 ~ 4.2V |
| Power turbine isentropic efficiency (DP) | 0.87 | Cell continuous maximum discharge current | 30A |
| Exhaust Pressure Ratio | 1.05 | Cell continuous maximum charge current | 5A |
| Shaft mechanical efficiency | 0.99 | Initial SOC | 100% |
| Gearbox efficiency | 0.97 | Minimum SOC requirement before descent | 90% |

## 5.3 Results and Analysis

A conventional baseline sizing optimization method is established for comparison. This baseline adopts a fixed-mass assumption, whereby the aircraft mass is treated as constant throughout the mission. The engine is represented using a reduced-order formulation without detailed fuel consumption coupling or operation strategy optimization. Under these assumptions, system sizing is conducted under identical mission profiles and energy management strategy settings, ensuring a consistent operational basis for comparison between the proposed FMOSO framework and the baseline method. The optimization is performed using the same constraint set and mission requirements for both approaches.

The optimization results of component sizing are summarized in Table 5. It can be observed that the $P_{\mathrm{TGS,DP}}$ is nearly identical for both methods, primarily because the cruise phase dominates the mission profile and thus governs the design-point power for TGS. The baseline method yields a slightly higher design-point power for the TGS, as the neglect of fuel mass variation leads to a higher power demand during the cruise phase. It is also found that both methods converge to the same $\pi_c$ and $T_{t4}$, with both parameters reaching their respective upper constraint limits. This indicates that, within the considered design space, a higher pressure ratio combined with a higher combustor exit temperature leads to improved thermal efficiency of the turboshaft engine, thereby enhancing fuel economy. Furthermore, both methods yield identical generator design-point parameters, which do not correspond to the maximum-efficiency operating point, but rather represent a trade-off between efficiency and mass. This suggests that the generator sizing is driven by a system-level mass–efficiency compromise rather than local peak-efficiency operation. In addition, the FMOSO-based design results in a lower number of battery cells in the battery pack. This indicates that, when fuel mass variation and operating strategy optimization are explicitly considered, the required power support from the battery is reduced, thereby avoiding unnecessary oversizing of the BESS.

Table 5 – Optimization results of component sizing.

| Method | $\pi_c$ | $T_{t4}$ / K | $P_{\mathrm{TGS,DP}}$ / kW | $n^*_{\mathrm{gen}}$ | $\tau^*_{\mathrm{gen}}$ | $N_s$ | $N_p$ | Total mass / kg |
|---|---|---|---|---|---|---|---|---|
| FMOSO framework | 9.5 | 1300 | 147.5 | 1 | -0.85 | 136 | 26 | 388.1 |
| Baseline method | 9.5 | 1300 | 148.3 | 1 | -0.85 | 152 | 24 | 400.8 |

The detailed comparison of the component-level mass distribution between the proposed FMOSO framework and the baseline method is further illustrated in Figure 9. As shown in the figure, the FMOSO framework achieves a total system mass reduction of 12.7 kg, primarily attributed to reductions in both battery pack mass and fuel mass. These results demonstrate that the proposed FMOSO framework enables a more accurate optimal sizing solution, effectively mitigating oversizing in key power components.

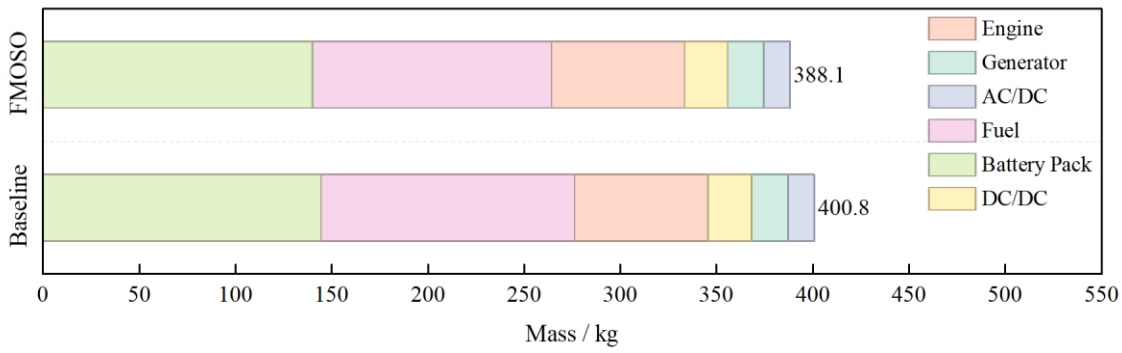



Figure 9 – Comparison of component mass distribution.

The energy consumption distribution across different mission phases is presented, as shown in Figure 10. It can be observed that, for both methods, the cruise phase accounts for the largest proportion of total energy consumption, thereby playing a dominant role in determining the TGS

sizing. In contrast, although the vertical take-off and transition phases are characterized by high power demand, their relatively short duration results in lower overall energy consumption, making them more influential on the BESS design. For the FMOSO-based design, the reduced aircraft mass during the cruise phase leads to a lower power requirement compared with the baseline method, which consequently decreases the corresponding energy consumption. This reduction further translates into a lower required fuel mass.

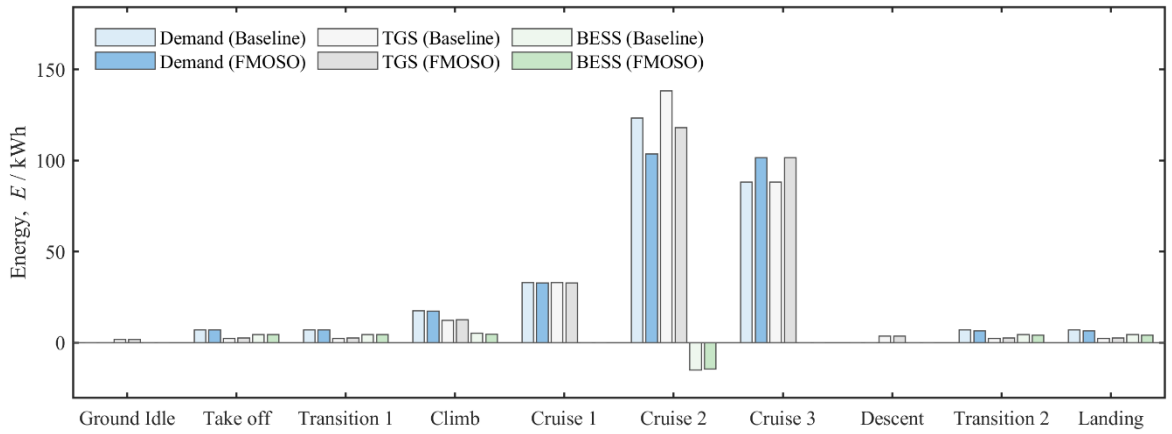



Figure 10 – Comparison of energy consumption distribution across mission phases between FMOSO and the baseline method

The optimal sizing results obtained using the proposed FMOSO framework are evaluated across the complete mission profile. Figure 11 illustrates the time histories of aircraft mass and DC bus power demand over the entire mission. The aircraft mass decreases almost linearly during cruise, indicating the engine fuel flow remains relatively stable. In contrast, steeper mass reduction is observed during take-off, transition, and landing phases, corresponding to higher engine fuel consumption under off-design conditions. For the DC bus power demand, a clear dependence on mission phase and aircraft mass is observed. The cruise-end power level is approximately 8 kW lower than that at cruise start, while the vertical landing power is about 21 kW lower than that of take-off. These results indicate that the reduction in aircraft mass has a noticeable impact on power demand, particularly in highly power-sensitive flight segments.

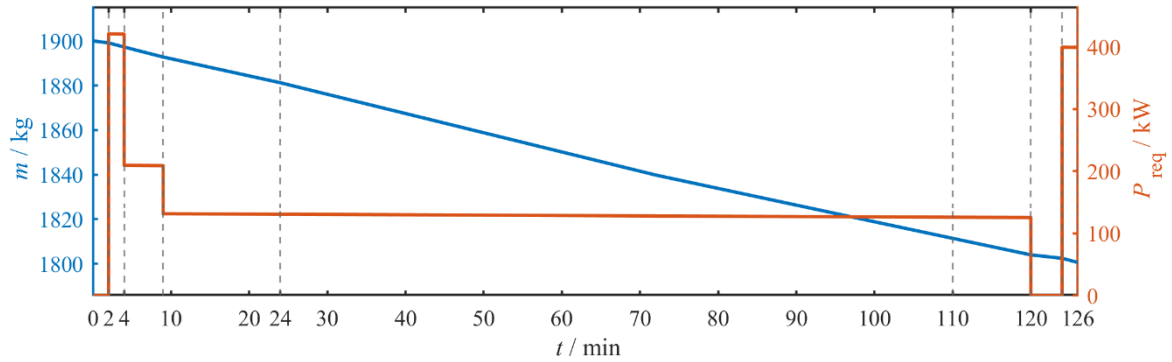



Figure 11 – Time evolution of aircraft mass and DC bus power demand.

Figure 12 presents the power split between the TGS and BESS throughout the mission. Under the proposed energy management strategy, the TGS operates in power-following mode during cruise and subsequently transitions to a charging mode, allocating surplus power to the BESS, after which it returns to power-following mode. During the climb and descent phases, the TGS exhibits pronounced nonlinear power variations, which is capable of representing the effects of altitude and velocity variations on the MCP capability of the TGS. Meanwhile, the BESS provides auxiliary power support to the TGS during high-power-demand phases, thereby reducing peak loading and helping maintain the TGS near its high-efficiency operating region.

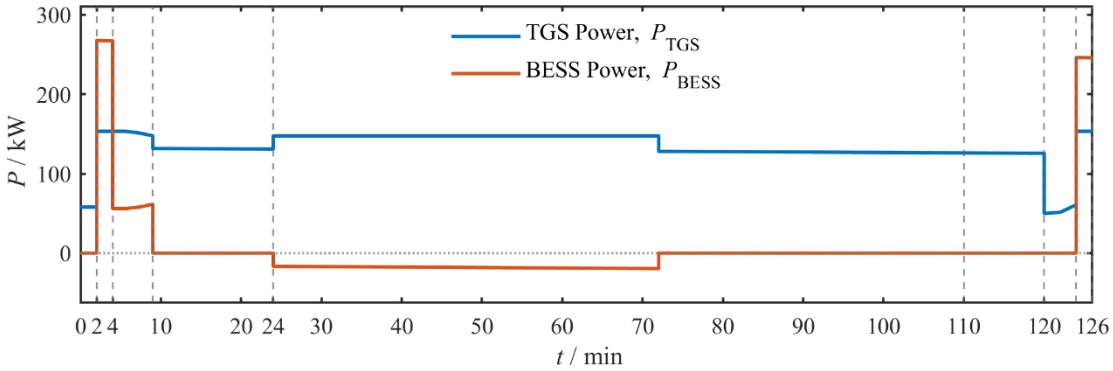



Figure 12 – Time evolution of power in the TGS and BESS.

Figure 13 shows the temporal evolution of SOC and C-rate, reflecting the dynamic charging and discharging behavior of the BESS. During the vertical take-off and transition phases, the BESS operates under high power output conditions, leading to a rapid decrease in SOC and a continuous increase in discharge C-rate. This behavior is primarily attributed to the SOC-dependent voltage drop: as SOC decreases, the OCV declines, and under an approximately constant power demand, the system compensates by increasing the discharge C-rate. The operating point approaches the discharge rate constraint boundary at the end of this phase. During the climb phase, the discharge C-rate exhibits a non-monotonic trend, decreasing first and then increasing. This behavior results from the combined effects of several mechanisms, including a slight variation in BESS power demand induced by altitude-dependent changes in TGS power output, polarization relaxation due to current step-down at the onset of the climb phase, and the gradual decrease in OCV as SOC decreases. In the cruise phase, governed by the energy management strategy, the battery first undergoes a recovery period, followed by a charging mode in which the TGS supplies energy to the BESS. The SOC then gradually increases and reaches the prescribed upper limit at approximately 72 minutes. By comparing the battery sizing results obtained from the FMOSO and baseline methods, it can be further observed that the peak battery discharge C-rate at the end of the transition phase (i.e., at 240 s) plays a critical role in determining the series–parallel configuration of the battery pack. In both cases, the operating point at 240 s approaches the allowable discharge C-rate limit, indicating that this condition is a key sizing constraint for the BESS. However, due to the consideration of fuel mass variation in the FMOSO framework, the overall aircraft mass at this time instant is reduced, leading to a lower power demand. In addition, the optimized MCP operation strategy for TGS enables a higher power contribution. As a result, the required power supplied by the BESS at this critical time instant is reduced, which in turn leads to a lower number of battery cells and a reduced battery pack mass compared with the baseline design.

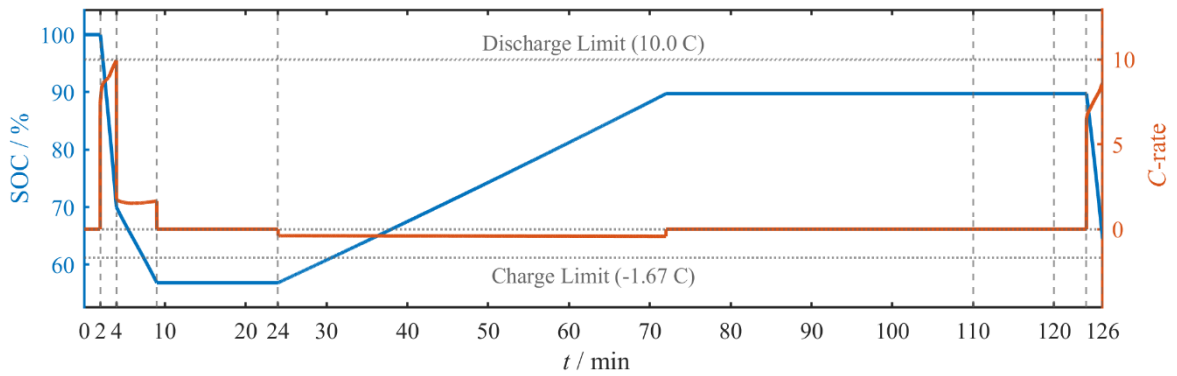



Figure 13 – Time evolution of battery pack SOC and C-rate.

## 6. Conclusion

In this study, a fuel-burn-aware mission-based sizing optimization framework is proposed and applied to the turboshaft-based series hybrid electric propulsion system of a RAM-oriented tiltrotor aircraft. A high-fidelity turboshaft thermodynamic model is adopted to represent engine performance,

while fuel-burn-induced aircraft mass variation and turboshaft–generator operation strategy optimization are incorporated into a unified time-stepping simulation framework, this method enables the representation of multidisciplinary coupling among aircraft mass evolution, power demand, and hybrid power system operation over the entire mission profile. A comparative analysis with a conventional fixed-mass baseline approach, which employs a reduced-order engine model without explicit fuel–mass coupling or operation strategy optimization, yields the following key conclusions:

i) The FMOSO framework considers fuel-burn-induced mass variation and turboshaft-generator operation strategy optimization, improving sizing fidelity and reducing oversizing. Compared to the baseline, it achieves a 12.7 kg mass reduction, mainly due to more accurate cruise power estimation reducing fuel mass requirements, and optimized MCP operation that lowers peak battery power demand. Generator sizing reflects a system-level mass–efficiency trade-off. Within the design space, thermal efficiency is driven by higher $\pi_c$ and $T_{t4}$, while the engine design point power is mainly dictated by the cruise phase.

ii) For the FMOSO-based design, aircraft mass reduction significantly influences power demand. Cruise-end power is ~8 kW lower than at start, and vertical landing power is reduced by ~21 kW relative to take-off, highlighting the importance of mass–power coupling in VTOL sizing.

iii) The peak battery discharge C-rate at 240 s (transition end) is identified as the key BESS sizing constraint. Under FMOSO, reduced mass and MCP operation strategy optimization reduce peak power demand for BESS, allowing a smaller battery pack within constraints.

## 7. Contact Author Email Address

Please contact the author at shen_guangjun@mail.nwpu.edu.cn

## 8. Copyright Statement

The authors confirm that they, and/or their company or organization, hold copyright on all of the original material included in this paper. The authors also confirm that they have obtained permission, from the copyright holder of any third party material included in this paper, to publish it as part of their paper. The authors confirm that they give permission, or have obtained permission from the copyright holder of this paper, for the publication and distribution of this paper as part of the ICAS proceedings or as individual off-prints from the proceedings.

## References

[1] Alam MI, Thu ZW, Nguyen N, Tyan M and Lee J-W. Integrated propulsion system analysis framework for designing advanced air mobility aircraft. *IEEE Transactions on Transportation Electrification*, Vol. 10, No. 4, pp 10219–10238, 2024.

[2] Johnson W and Silva C. NASA concept vehicles and the engineering of advanced air mobility aircraft. *Aeronautical Journal*, Vol. 126, No. 1295, pp 59–91, 2022.

[3] Viswanathan V, Epstein AH, Chiang Y-M, Takeuchi E, Bradley M, Langford J and Winter M. The challenges and opportunities of battery-powered flight. *Nature*, Vol. 601, No. 7894, pp 519–525, 2022.

[4] Yang X-G, Liu T, Ge S, Rountree E and Wang C-Y. Challenges and key requirements of batteries for electric vertical takeoff and landing aircraft. *Joule*, Vol. 5, No. 7, pp 1644–1659, 2021.

[5] Ugwueze O, Statheros T, Horri N, Bromfield MA and Simo J. An efficient and robust sizing method for evtol aircraft configurations in conceptual design. *Aerospace*, Vol. 10, No. 3, pp 311, 2023.

[6] Bærheim T, Lamb JJ, Nøland JK and Burheim OS. Potential and limitations of battery-powered all-electric regional flights—a norwegian case study. *IEEE Transactions on Transportation Electrification*, Vol. 9, No. 1, pp 1809–1825, 2023.

[7] KANG L, RAN Q, MAO J, YU Z and HAN F. Hybrid propulsion systems and aircraft digital design status and prospects. *Journal of Propulsion Technology*, Vol. 45, No. 3, pp 89–105, 2024.

[8] Friedrich C and Robertson PA. Design of hybrid-electric propulsion systems for light aircraft. Proc *AIAA AVIATION Forum*, Atlanta, GA, 2014.

[9] Li Y, Li H, Xie G and Tao Z. Configuration trade-off and co-design optimization of hybrid-electric vtol propulsion systems. *Drones*, Vol. 9, No. 11, pp 800, 2025.

[10] Dehghani M, Baei MA, Khazaee M, Zahedifar F and Khoee AG. Sizing of power storage and conversion components in a hybrid electric propulsion system for advanced air mobility. *Journal of Power Sources*, Vol. 640, pp 236681, 2025.

[11] Zong J, Zhu B, Hou Z, Yang X and Zhai J. Sizing and mission profile analysis of the hybrid-electric propulsion

system for retrofitting a fixed wing vtol aircraft. *International Journal of Aerospace Engineering*, Vol. 2022, pp 1–10, 2022.

[12] Meng X, Wang T and Wu L. Optimal power allocation-based sizing method with high computation efficiency for fuel cell emu intercity train considering the power source degradation. *IEEE Transactions on Transportation Electrification*, Vol. 12, No. 2, pp 2086–2096, 2026.

[13] Tianmu J, Xiaobo Z and Zhanxue W. Modelling and control schedule design of turbo- electric propulsion system. *Journal of Propulsion Technology*, Vol. 45, No. 1, pp 23–35, 2024.

[14] YI W, CUI Z and ZHENG T. Effect investigation of combined variable speed of rotor/turboshaft engine power turbine on the performance. *Journal of Aerospace Power*, Vol. 39, No. 9, pp 131–140, 2024.

[15] Fu Y, Liu ZW and Zheng TH. Turbo-electric hybrid aero propulsion system key technologies analysis. *Journal of Propulsion Technology*, Vol. 45, No. 3, pp 2208034, 2024.

[16] Zou W and Zheng X. Development trends of aero turboshaft engines. *Journal of Aerospace Power*, Vol. 34, No. 12), pp 2577–2588, 2019.

[17] Bell ME and Litt JS. An electrical modeling and thermal analysis toolbox for electrified aircraft propulsion simulation. Proc *AIAA Propulsion and Energy 2020 Forum*, VIRTUAL EVENT, 2020.

[18] Pellegrino G, Vagati A, Boazzo B and Guglielmi P. Comparison of induction and pm synchronous motor drives for ev application including design examples. *IEEE Transactions on Industry Applications*, Vol. 48, No. 6, pp 2322–2332, 2012.

[19] Wang Y, Tian J, Sun Z, Wang L, Xu R, Li M and Chen Z. A comprehensive review of battery modeling and state estimation approaches for advanced battery management systems. *Renewable and Sustainable Energy Reviews*, Vol. 131, pp 110015, 2020.

[20] Ramsey D, German R, Bouscayrol A and Boulon L. Comparison of equivalent circuit battery models for energetic studies on electric vehicles. Proc *2020 IEEE Vehicle Power and Propulsion Conference (VPPC)*, pp 1–5, 2020.

[21] Thakkar RR, Rao YSrinivasa and R.Sawant R. Performance analysis of electrical equivalent circuit models of lithium-ion battery. Proc *2020 IEEE Pune Section International Conference (PuneCon)*, Pune, India, pp 103–107, 2020.

[22] Menzi D, Imperiali L, Bürgisser E, Ulmer M, Huber J and Kolar JW. Ultralightweight high-efficiency buck-boost dc-dc converters for future evtol aircraft with hybrid power supply. *IEEE Transactions on Transportation Electrification*, Vol. 10, No. 4, pp 10297–10313, 2024.

[23] Burguburu S and Basset P-M. Turboshaft engine predesign and performance assessment. Proc *48th AIAA/ASME/SAE/ASEE joint propulsion conference & exhibit*, 2012.

[24] Sayed E, Abdalmagid M, Pietrini G, Sa'adeh N-M, Callegaro AD, Goldstein C and Emadi A. Review of electric machines in more-/hybrid-/turbo-electric aircraft. *IEEE Transactions on Transportation Electrification*, Vol. 7, No. 4, pp 2976–3005, 2021.

[25] Ghosh S, Das S, Vasilakos AV and Suresh K. On convergence of differential evolution over a class of continuous functions with unique global optimum. *IEEE Transactions on Systems, Man, and Cybernetics Part B: Cybernetics*, Vol. 42, No. 1, pp 107–124, 2012.

[26] Hao W, Wang Z and Zhang X. Solving variable cycle engine model based on adaptive differential evolution algorithm. *J. Propul. Technol.*, Vol. 42, No. 9, pp 2011–2021, 2021.

[27] Kiesewetter L, Shakib KH, Singh P, Rahman M, Khandelwal B, Kumar S and Shah K. A holistic review of the current state of research on aircraft design concepts and consideration for advanced air mobility applications. *Progress in Aerospace Sciences*, Vol. 142, pp 100949, 2023.

[28] Kim Y and Kang S. Techno-economic analysis of fuel cell-battery hybrid urban air mobility. *Applied Thermal Engineering*, Vol. 297, pp 130787, 2026.

[29] Moller PS and Eng M. Performance evaluation of select personal air vehicles. *Freedom-Motors. Com*, 2020.

[30] Zhao X, Liu Y, Yang Z, Wang R, Liu L, Wang L and Wang Y. A modified high c-rate battery equivalent circuit model based on current dependence and concentration modification. *Electrochimica Acta*, Vol. 478, pp 143833, 2024.